PCCP

Accepted Manuscript

ROYAL SOCIETY OF CHEMISTRY

www.rsc.org/pccp

Cite this: DOI: 10.1039/c0xx00000x

www.rsc.org/xxxxxx

ARTICLE TYPE

Electronic structure study of $Ce_{1-x}A_xO_2$ (A = Zr & Hf) Nanoparticles: NEXAFS and EXAFS investigations

Aditya Sharma[a], Mayora Varshney[a], Hyun-Joon Shin[a], Yong Jun Park[a], Min-Gyu Kim[a] Tae-Kyun Ha[a], Keun Hwa Chae[b] and Sanjeev Gautam[a,bψ]

Received (in XXX, XXX) Xth XXXXXXXXX 20XX, Accepted Xth XXXXXXXXX 20XX

DOI: 10.1039/b000000x

Single phase nanoparticles (NPs) of CeO_2, $Ce_{0.5}Zr_{0.5}O_2$, $Ce_{0.5}Hf_{0.5}O_2$ and $Ce_{0.5}Hf_{0.25}Zr_{0.25}O_2$ were successfully synthesized by co-precipitation method at constant pH and temperature. The X-ray diffraction results revealed that the additive atoms did not segregate to form secondary phases but lead to grain size variation in the NPs. The 10 Dq values in the near edge X-ray absorption fine structure (NEXAFS) spectra at the O K-edge did not vary in the same way as the average grain size was changed for the doped CeO_2 NPs. The de-convolution of Ce M_5-edge and detailed analysis of O K pre-edge peak have shown the higher $Ce^{+3}/(Ce^{+3}+Ce^{+4})$ ratio in the Zr and Hf doped samples. The local atomic structure around the Ce, Zr and Hf atoms was investigated by using extended X-ray absorption fine structure (EXAFS) spectroscopy at Ce K-edge, Zr K-edge and Hf L_3-edge, respectively, and the EXAFS data were fitted with the theoretical calculations. The *4f* occupancy, $Ce^{+3}/(Ce^{+3}+Ce^{+4})$ ratio of Ce ions, coordination number of Ce and Ce-Ce/Ce-O bond distances were sensitive to the additive atoms but not explicitly changed according to the grain size variation in the NPs.

Introduction

The *f*-cell electrons of Ce based compounds make them appealing for their extraordinary physical/chemical properties and technological importance [1-3]. In the recent years, there have been efforts to boost catalytic activity [4-5], solid oxide fuel cell performance [6] and magnetic properties [7-8], of CeO_2. In all such reports the aim was to create either larger surface area of nanoparticles (NPs) or O vacancies in the CeO_2 samples. The mixed valence state of Ce (i.e., Ce^{+3} and Ce^{+4}), caused by the formation of O vacancies, certainly enhanced the charge transfer transitions between O *2p* and Ce *4f* bands through the double exchange mechanism and thus favored the ferromagnetism in the nanocrystalline CeO_2 [7-8]. Besides this, the oxygen vacancies and mixed valence state of Ce have also been reported to enhance the ability of releasing or uptaking the oxygen under the reduction or oxidation conditions, respectively, and consequently have improved the oxygen storage capacity (OSC)/three-way-catalyst (TWC) performance of CeO_2 [9-12]. Highly oxygen deficient CeO_2 systems have been synthesized by the incorporation of isovalent (Zr^{+4}, Hf^{+4} and Sn^{+4} etc.) [13-15] and aliovalent (Ca^{+2}, Cu^{+2}, Zn^{+2}, Ni^{+2}, Fe^{+2} etc.) elements [16-17]. The concentration of O vacancies and valence state of Ce are not only dependant on the valence state of additive atoms but also modified by the size of the dopants. For the aliovalent dopants the O vacancy can be introduced due to the charge compensation mechanism. However, it can also be formed due to the lattice distortion or strain in case of aliovalent additives. Therefore, maneuvering and determining the O concentration and valence state of Ce may have important implications on the exploration of diverse properties of CeO_2.

Nevertheless, the additive atoms enhance the OSC and thus TWC performance of CeO_2 by creating O vacancies and active redox couples of Ce^{+3} and Ce^{+4}. But, in some of the previous reports, the incorporation of such dopants leads to decrease in the grain size of oxide NPs [15-16, 18]. This effect becomes severe when the doping concentrations are large [18]. In such conditions, it is questionable that the observed changes in the concentration of O vacancy and chemical state of the metal ions either belong to the size-confinement effects or doping effects. Therefore, comprehensive studies on the synthesis and electronic structure determination of pure and binary-doped CeO_2 NPs are desirable for the abundant understanding of the size-confinement, crystal structure and chemical bonding effects. Besides this, the combination of two metal elements in the CeO_2 matrix can produce new compounds with novel structural/electronic structure properties and catalytic activity.

The X-ray photoelectron spectroscopy (XPS) technique is widely reported for determining the Ce^{+3}/Ce^{+4} concentrations in the doped CeO_2 systems [11, 13-15]. On the other hand, the X-ray absorption spectroscopy (XAS) which is an element specific tool for the determination of charge state, coordination number and hybridization of the probed atom, has not been extensively reported for such compounds [15-16]. Furthermore, XPS analysis has been shown to overestimate the Ce^{+3} concentrations than that of estimated by XAS [19]. Most of the previous reports, on the XAS studies of doped CeO_2, have concerned on either O K-edge or Ce L-edge [16, 19-20]. In case of extended X-ray absorption fine structure (EXAFS) analysis at Ce L_3-edge the accuracy of derived structural parameters was lower due to limited data range because of the small separation between L_3 and L_2-edges. Furthermore, there have been two undesired phenomena, (i) final state mixing with valence state and (ii) multi-electron excitation which interface with the L_3 EXAFS analysis [20]. It has been found that EXAFS analysis at Ce K-edge is simpler and more straightforward than the procedures for Ce L_3-EXAFS [21]. More accurate local structure around Ce atom can be obtained because of larger EXAFS data range and hence a better resolution between the contributions from different coordination shells.

In this study, we examined the XAS (within the soft and hard X-ray region) of chemically synthesized CeO_2 NPs, which were doped with Zr and Hf at constant concentrations ($x=0.5$). NEXAFS measurements at O K-edge and Ce $M_{5,4}$-edge have shown that the *4f* occupancy and, thus, $Ce^{+3}/(Ce^{+3}+Ce^{+4})$ ratios have been increased in the doped NPs. The local atomic structure determination, with the help of Ce K-edge EXAFS, around the Ce atom has shown the variations in the coordination number and

bond distances. This work has also attempted to add an understanding on the atomic structure and electronic structure properties of CeO_2 which were analyzed as a function of Hf and Zr doping and changes in the grain size of NPs.

Experimental details

Pure and doped CeO_2 NPs were synthesized using a previously established, co-precipitation, method [22-23]. All the reagents used were of analytical grade without further purification. For the synthesis of pure CeO_2 NPs, the $Ce(CH_3COO)_3.5H_2O$ (Aldrich, 99.9 purity) was mixed into double distilled (DI) water with stirring at room temperature. When the precursor had been totally dissolved the diluted NH_4OH solution was, drop-wise, added into the precursor. The reaction was done at 9 pH value of the solution under the constant stirring. The precipitates were washed several times with DI water and then dried at 80 °C in air for 30 hours to obtain fine powdered sample. To obtain the Hf and Zr doped CeO_2 NPs, the clear solutions of $ZrCl_4.5H_2O$ and $HfCl_4.5H_2O$ were added at the same time into the clear solutions of $Ce(CH_3COO)_3.5H_2O$ and then stirrer for 30 min. Doping (Hf or Zr = A) ratio was the molar ratio of *A* to *A+Ce*, namely *x*. The doping concentration (x = 0.5), pH value of solution, heating time, heating temperature and stirring speed were kept constant to prepare (i) CeO_2, (ii) $Ce_{0.5}Zr_{0.5}O_2$, (iii) $Ce_{0.5}Hf_{0.5}O_2$ and (iv) $Ce_{0.5}Hf_{0.25}Zr_{0.25}O_2$ NPs. Therefore, the modifications in the structural and electronic structure properties are to be analyzed as a consequence of doping element effects and not due to the other factors like; pH value and temperature etc. The as-prepared samples were characterized using the synchrotron X-ray diffraction (λ = 1.240 Å) performed at X-ray scattering beam line (3D beam line of Pohang Accelerator laboratory (PAL), South Korea). The morphology and crystallite sizes were studied with FEI-Tecnai-20 transmission electron microscope (TEM) accompanied with selected area electron diffraction (SAED) and energy dispersive X-ray spectroscopy (EDS). Near edge X-ray absorption fine structure (NEXAFS) spectra at the O K-edge and Ce $M_{5,4}$-edge were collected in the total electron yield (TEY) mode at 10D (PAL-KIST) beam line. The photon energy resolution of this beam line was better than 0.6 eV (at O K-edge). The extended X-ray absorption fine structure (EXAFS) measurements at Ce K-edge, Zr K-edge and Hf L_3-edge were performed at 10 C beam line of PAL. This beam line has high flux and wide energy range with a Si (311) double crystal monochromator. Higher harmonics were effectively removed by detuning of the crystals to 70% of the maximum intensity. Three ionization chambers, filled with Ar gas, were used to record the intensity of the incident and the transmitted X-rays (the sample is placed between the first and second ionization chamber).

Results and discussion

Fig. 1 shows the XRD patterns of CeO_2, $Ce_{0.5}Zr_{0.5}O_2$, $Ce_{0.5}Hf_{0.5}O_2$ and $Ce_{0.5}Hf_{0.25}Zr_{0.25}O_2$ NPs. The diffraction peaks were indexed according to the cubic fluorite structure with the space group of Fm3m (JCPDS# 34-0394). No diffraction peaks from the impurity phases, such as Ce_2O_3, ZrO_2, HfO_2 etc., could be detected within the detection limit of used X-ray diffractometer. This indicates that the dopants do not segregate but occupy the Ce cites in the CeO_2 lattice. A closer look of the diffraction patterns reveals that a significant XRD peak broadening is present, particularly, in the doped samples. Several possibilities can explain the peak broadening like; decrease in the grain size and distorted crystal structure etc.

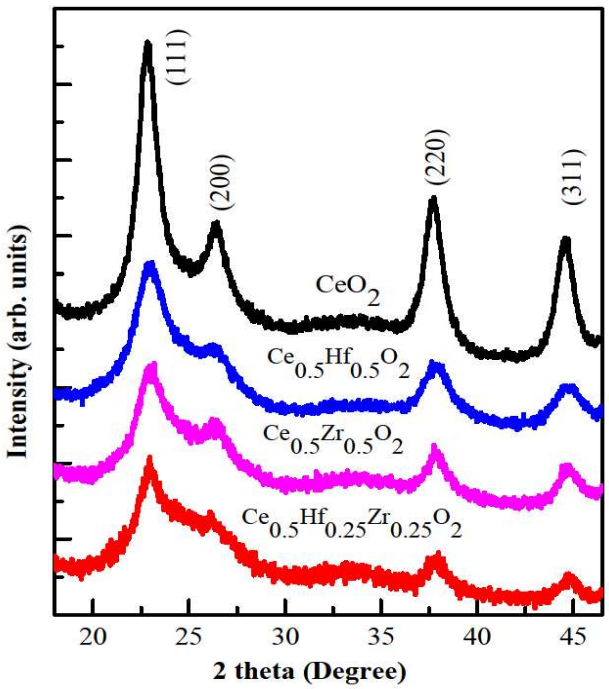

Fig. 1. (colour online) X-ray diffraction patterns of CeO_2, $Ce_{0.5}Zr_{0.5}O_2$, $Ce_{0.5}Hf_{0.5}O_2$ and $Ce_{0.5}Hf_{0.25}Zr_{0.25}O_2$ NPs. (The base lines were displaced vertically for clarity).

The average grain size was calculated using the Scherrer relation ($D = 0.9\,\lambda/(\beta\,Cos\theta$, where D is the average grin size, β is the full width at half maximum of the XRD peek and λ is the wavelength of used X-rays) and presented in the Fig. 2 (a). It is clear from the Fig. 2(a) that the grain size of pure CeO_2 is ~5 nm which reduced to ~ 2.5 nm for the doped samples. To further confirm the size and morphology of the NPs, systematic, TEM measurements were performed on the samples. Fig. 3(a), (b), (c) and (d) show the TEM images of pure, Zr doped, Hf doped and Zr+Hf doped CeO_2 NPs, respectively. The selected area electron diffraction (SAED) patterns of each sample are also provided in the inset of their respective TEM image. It is clear from the Fig.3 that all the samples show the spherical morphology of NPs with the average diameter of ~ 5 nm. The encircled area in the TEM images shows the closer view of the particle and orientation of the crystallographic planes. Further, the ring patterns in the SAED images are also convening the crystalline nature of all the samples. However, aggregation of NPs is visible in all of the TEM images. Such aggregation is expected in the wet chemically synthesized samples due to the substantial presence of hydroxyl ions in the NPs [18, 22-23]. The size of NPs (~ 5 nm), obtained from TEM images, is quite diverse than that of XRD analysis. This may be due the fact that the TEM gives overall morphological size of the NPs and the XRD take care of the crystalline grain size (in which long range ordering is present). Similar decrease in the grain size has also been observed in the other oxide NPs [16, 18] because the doping induces local distortion in the crystalline lattice and restricts the long range ordering which, indeed, reflect in the XRD data. Further analysis has been done on the intensity ratio ($I_{(111)}/I_{(311)}$) of two XRD peaks (i.e., (111) and (311) peaks) to understand the doping effect on the crystal structure of the samples. It is clear from the Fig. 2 (b) that the $I_{(111)}/I_{(311)}$ ratio is less in the case of $Ce_{0.5}Zr_{0.5}O_2$ NPs and little higher in the case of $Ce_{0.5}Hf_{0.5}O_2$ and $Ce_{0.5}Hf_{0.25}Zr_{0.25}O_2$ NPs.

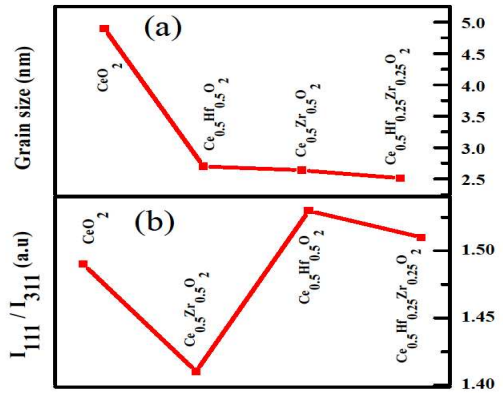

Fig. 2. (colour online) **(a)** average grain size and (b) intensity ratio $\{I_{(111)}/I_{(311)}\}$, calculated from the XRD patterns of CeO_2, $Ce_{0.5}Zr_{0.5}O_2$, $Ce_{0.5}Hf_{0.5}O_2$ and $Ce_{0.5}Hf_{0.25}Zr_{0.25}O_2$ NPs.

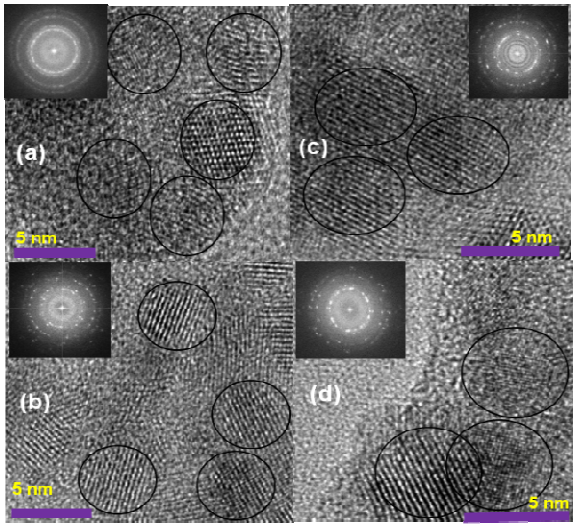

Fig. 3. (colour online) TEM images of (a) CeO_2, (b) $Ce_{0.5}Zr_{0.5}O_2$, (c) $Ce_{0.5}Hf_{0.5}O_2$ and (d) $Ce_{0.5}Hf_{0.25}Zr_{0.25}O_2$ NPs (insets show the SAED patterns of the respective sample).

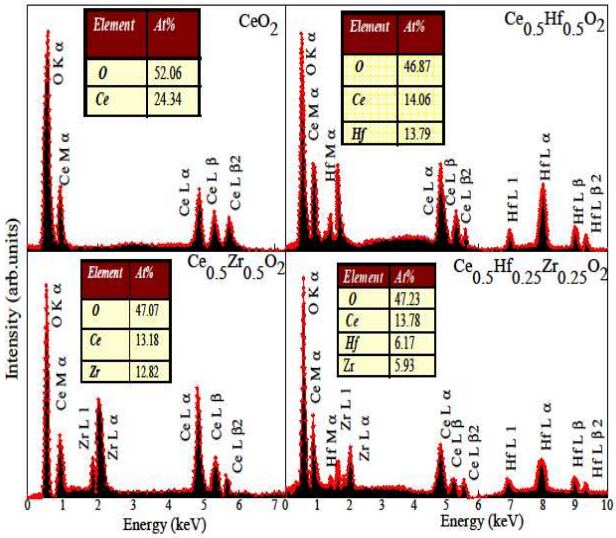

Fig. 4. (colour online) EDS spectra of CeO_2, $Ce_{0.5}Zr_{0.5}O_2$, $Ce_{0.5}Hf_{0.5}O_2$ and $Ce_{0.5}Hf_{0.25}Zr_{0.25}O_2$ NPs (insets show the atomic concentration of the elements in the respective sample).

The observed decrease/increase in the intensity ratio for Zr/Hf doped CeO_2 NPs may be ascribed to the substitution of Ce by Zr/Hf in the CeO_2 lattice. It may be noted here that the atomic scattering factor for Zr (Z = 40) is less than that of Ce (Z = 58) and, therefore, any substitution of Ce by Zr may lead to change in the structure factor of CeO_2 lattice. This reflects as the decrease in the XRD peak intensity ratio in the Zr doped sample. Similarly, the scattering factor of Hf (Z = 72) is little higher than that of Ce and, therefore, increase in the intensity ratio has been observed in the case of $Ce_{0.5}Hf_{0.5}O_2$ NPs. However, intensity ratio marginally decreases in $Ce_{0.5}Hf_{0.25}Zr_{0.25}O_2$ NPs and may be due to the presence of both Zr and Hf atoms in the CeO_2 lattice. Similar changes in the intensity ratio have also been reported in the Co doped SnO_2 NPs and signified the substitutional doping of Co in SnO_2 [22]. To further quantify the elemental concentrations in the as-synthesized NPs, systematic, EDS spectra have been collected and presented in the Fig.4. The peaks of Cu and C, which originate from the carbon coated Cu grids, are eliminated from the spectra for the sake of clarity of spectra. The element present in the samples and their atomic percentages are also listed in the inset of each panel. From the EDS data it is noticeable that atomic percentage of O is reduced in the doped samples and the atomic concentration of Ce, Zr and Hf is very close to each other. This is accordance to our synthesis procedure where we used the molar ratio of the constituent elements. The XRD results ruled out the possibility of the existence of the secondary phases and convinced the substitutional doping of Zr and Hf in CeO_2 lattice. However, further investigations may be advantageous to probe the local impurity phases (which do not have long range ordering) and local electronic structure of the NPs. In this regard the soft X-ray NEXAFS measurements have been collected at O K-edge and Ce $M_{5,4}$-edge and shall be discussed in the following sections.

In the case of cubic type compounds (i.e., CeO_2) the metal d_{xy}, d_{xz} and d_{yz} orbitals point towards the oxygen atoms, while the $d_{x^2-y^2}$ and d_{z^2} orbitals point between the ligands. As a result of this e_g (group of $d_{x^2-y^2}$ and d_{z^2}) orbital lowered in energy and the other orbital namely t_{2g} (group of the d_{xy}, d_{xz}, and d_{yz}) rose in energy [24]. The energy difference between e_g and t_{2g} is called crystal-field splitting parameter and represented by *10 Dq*. Fig. 5 presents the O K-edge spectra of CeO_2, $Ce_{0.5}Zr_{0.5}O_2$, $Ce_{0.5}Hf_{0.5}O_2$ and $Ce_{0.5}Hf_{0.25}Zr_{0.25}O_2$ NPs. All spectra were normalized to the intensity obtained at the energy of 565 eV. At this energy the electron transition takes place to the continuum states [16]. It is clear from the Fig. 5 that the O K-edge spectrum of pure CeO_2 NPs presents three intense peaks (represented by the letters A, B and C) positioned at 530.7 eV, 533.4 eV, and 537.6 eV, respectively. These peaks mainly arises because of the hybridization of O 2p states with the Ce *4f*, *5d* (e_g) and *5d* (t_{2g}) states, respectively [16, 25]. To get insight on the variation in the grain size (calculated by XRD), with Zr and Hf doping, the O K-edge spectra have been examined with respect to the two different factors; (i) doping effect and (ii) grain size effect. It is known that, because of the crystal field effects, the 10 Dq value exceeds in the case of small sized NPs [16, 24]. However, in the present case the 10 Dq of the doped CeO_2 NPs does not exceed over that of the pure CeO_2 NPs. Therefore, the observed changes in the XRD and O K-edge spectra are the consequences of doping effect rather than the differences in the size of NPs. The apparent change in the O K-edge spectra is the decrease in the intensity of peak *A* in all the doped CeO_2 NPs. The decrease in the intensity of peak *A* may be the consequence of the reduction of unoccupied *4f* states and indicates that the *4f* orbitals, in the doped NPs, are partially filled with the electrons. To quantify the variation of the intensity of peak *A*, the area under the peak was examined and presented in the inset of Fig. 5. It is clear from the inset of Fig. 5

that the area under the peak *A* is decreased, significantly, in the $Ce_{0.5}Zr_{0.5}O_2$ NPs and becomes constant for the $Ce_{0.5}Hf_{0.5}O_2$ and $Ce_{0.5}Hf_{0.25}Zr_{0.25}O_2$ NPs. This indicates that *4f* occupancy has been increased in $Ce_{0.5}Zr_{0.5}O_2$, $Ce_{0.5}Hf_{0.5}O_2$ and $Ce_{0.5}Hf_{0.25}Zr_{0.25}O_2$ NPs. Here, it is worth of mentioning that the doping concentration was kept constant (x= 0.5) for all the samples and therefore the *4f* occupancy is almost same for the Zr and Hf doped CeO_2 NPs. Interestingly, it is visible from the Fig. 5 that the energy separation between e_g and t_{2g} peaks is little lesser in the Zr doped NPs and, marginally, larger for the Hf doped NPs. This could be due the fact that the *5d* orbitals of Hf are more extended (in the case of Hf doped NPs), resulting in the extensive overlap with the O *2p* orbitals, and this leads to larger energy splitting in the e_g and t_{2g} orbitals. On the other hand, the *4d* orbitals of Zr (in the case of $Ce_{0.5}Zr_{0.5}O_2$ NPs) are not much extended (in comparison to *5d* orbitals of Hf and Ce), resulting in less overlapping with the O *2p* orbitals and less splitting in the e_g and t_{2g} orbitals. The O K-edge spectra from the NPs of pure ZrO_2 and HfO_2 were also collected to compare the spectral features with those of the CeO_2, $Ce_{0.5}Zr_{0.5}O_2$, $Ce_{0.5}Hf_{0.5}O_2$ and $Ce_{0.5}Hf_{0.25}Zr_{0.25}O_2$ NPs. It is also clear from the Fig. 5 that the spectral features of the pure and doped CeO_2 NPs are quite different from those of pure HfO_2 and ZrO_2 NPs. This strengthened our view of the unlikely formation of the trivial phases of ZrO_2 and HfO_2 in the doped CeO_2 NPs and tally with the findings of XRD measurements. Therefore, the O K- edge spectra of pure and doped CeO_2 NPs help us to conclude that the Hf and Zr do not form secondary phases in the CeO_2 lattice but modify the electronic structure by changing the number of unoccupied *4f* orbitals and hybridizing with the lattice oxygen. Furthermore, 10 Dq values of the doped samples do not exceed over that of pure CeO_2 NPs and thus neglect the grain size effects in the electronic structure of the doped samples. It is known that, because of the large overlap of the O *2p* and Ce *4f* wave functions, the pre-edge peak (peak *A*) in the O K-edge yields the density of Ce *4f* states in CeO_2 [16, 24, 25]. Since, the Ce $M_{5,4}$-edge XAS of CeO_2 corresponds to the electron transition from the Ce $3d_{3/2}$ and $3d_{5/2}$ core levels into the *4f* unoccupied electronic states. Therefore, Ce $M_{5,4}$-edge XAS directly reflects the occupancy of the *4f* orbital [26].

To understand such facts in the present study, systematic, Ce $M_{5,4}$-edge spectra were collected from the pure and doped CeO_2 NPs and presented in the Fig. 6. To further clarify the +3 valence state of cerium, Ce $M_{5,4}$-edge XAS spectrum was also collected from the standard $CeAl_2$ powders (Ce is regarded as tetravalent (Ce^{+4}) in CeO_2 and trivalent (Ce^{+3}) in $CeAl_2$ [16]) and plotted along with the spectra of as-synthesized samples. It is clear from the Fig. 6 that the pure CeO_2 NPs show two major peaks at ~ 885.1 eV and ~ 902.9 eV for Ce M_5-edge and M_4-edge, respectively. Besides this, there are two post edge peaks at ~ 890.3 eV and 908.1 eV, respectively. The spectral features of the as-synthesized samples resemble to those of typical CeO_2 NPs [16, 26] and, thus, validate the synthesis of good quality samples in the present study. In the first sight, all as-synthesized NPs exhibit mixed +4 and +3 valence states of Ce. This is because of the fact that the spectral features of Ce $M_{5,4}$-edge spectra of pure and doped CeO_2 NPs, partially, match with the spectral features of $CeAl_2$, except that the pure and doped CeO_2 NPs exhibit two post edge peaks *P* and *P**. Generally, the Ce M_4-edge follows the Ce M_5-edge and treated as the replica of the Ce M_5-edge. Therefore, for the sake of convenience, we de-convoluted the Ce M_5-edge, along with the peak P (see Fig. 7). The post edge peaks, *P* and P^*, are the indicative of the contribution of $4f^0$ states, because these peaks arise from the transitions to *4f* states in the conduction band [26].

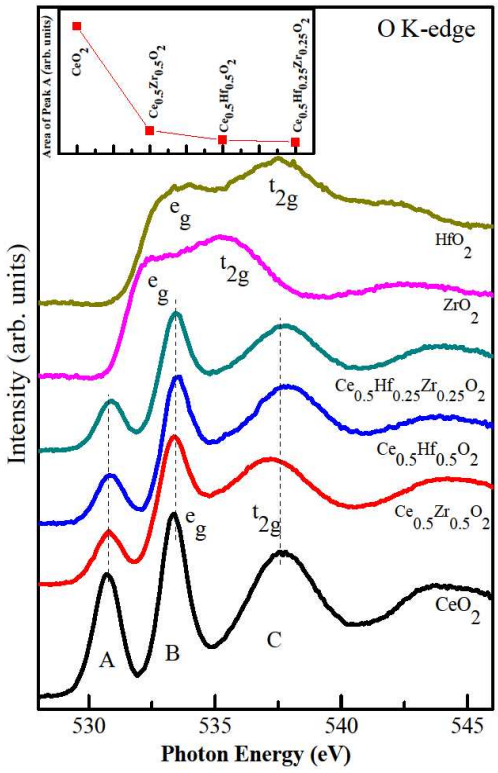

Fig. 5. (colour online) O K-edge NEXAFS spectra of CeO_2, $Ce_{0.5}Zr_{0.5}O_2$, $Ce_{0.5}Hf_{0.5}O_2$ and $Ce_{0.5}Hf_{0.25}Zr_{0.25}O_2$ NPs. Inset shows the variation in the intensity of peak A.

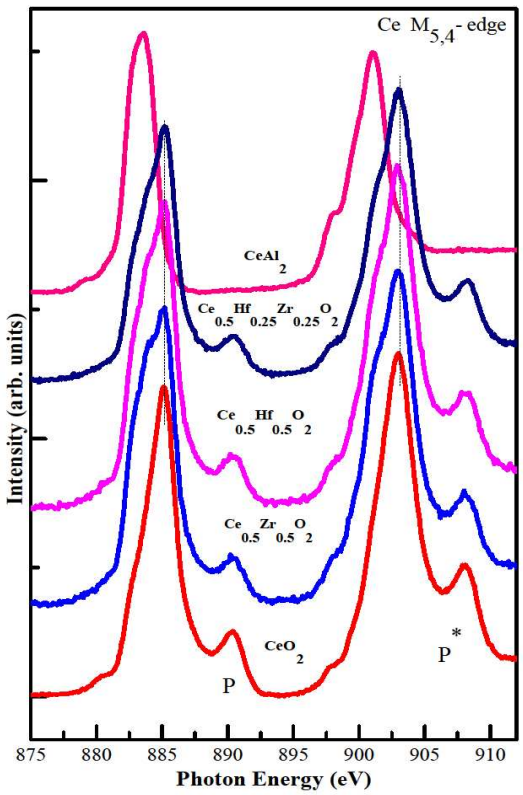

Fig. 6. (colour online) Ce $M_{5,4}$-edge NEXAFS spectra of $CeAl_2$, CeO_2, $Ce_{0.5}Zr_{0.5}O_2$, $Ce_{0.5}Hf_{0.5}O_2$ and $Ce_{0.5}Hf_{0.25}Zr_{0.25}O_2$ NPs.

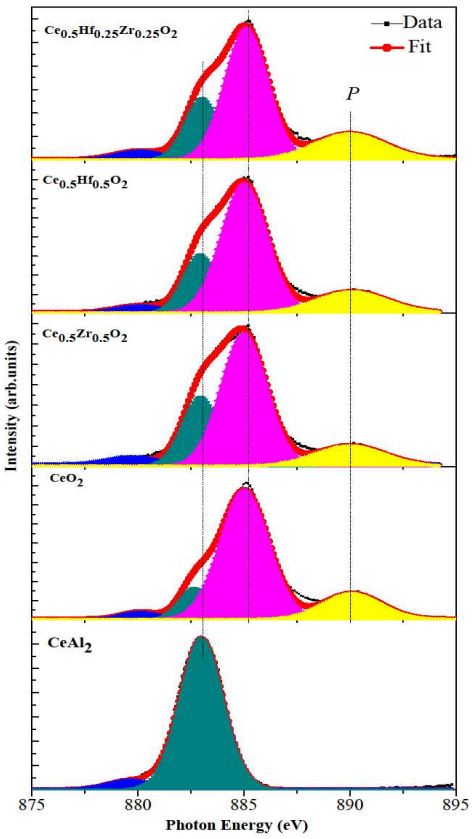

Fig.7 (colour online) de-convoluted Ce M_5-edge spectra of $CeAl_2$, CeO_2, $Ce_{0.5}Zr_{0.5}O_2$, $Ce_{0.5}Hf_{0.5}O_2$ and $Ce_{0.5}Hf_{0.25}Zr_{0.25}O_2$ NPs

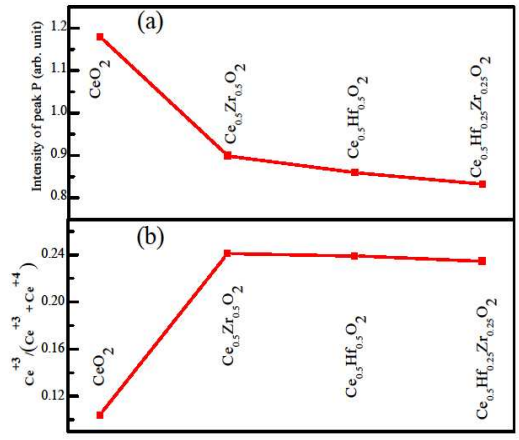

Fig. 8. (colour online) (a) variation in the intensity of peak *P* and (b) $Ce^{+3}/(Ce^{+3}+Ce^{+4})$ ratios (calculated from the Ce M_5-edge spectra) for CeO_2, $Ce_{0.5}Zr_{0.5}O_2$, $Ce_{0.5}Hf_{0.5}O_2$ and $Ce_{0.5}Hf_{0.25}Zr_{0.25}O_2$ NPs

The $CeAl_2$ (Ce in +3 valence state) does not exhibit such post edge peaks. Therefore the intensity of *P* or P^* can be used to estimate the amount of $4f^0$ states. Fig. 8 (a) and 8 (b) represents the variation in the intensity of peak *P* and $Ce^{+3}/(Ce^{+3}+Ce^{+4})$ ratios, respectively. It is clear from the Fig. 8 (a) that the intensity of *P* peak, gradually, decreased for the $Ce_{0.5}Zr_{0.5}O_2$ NPs and then almost constant for the $Ce_{0.5}Hf_{0.5}O_2$ and $Ce_{0.5}Hf_{0.25}Zr_{0.25}O_2$ NPs. On the other hand, the $Ce^{+3}/(Ce^{+3}+Ce^{+4})$ ratio increased for the $Ce_{0.5}Zr_{0.5}O_2$ NPs and then almost saturated for $Ce_{0.5}Hf_{0.5}O_2$ and $Ce_{0.5}Hf_{0.25}Zr_{0.25}O_2$ NPs. The change in electronic configuration from Ce^{+4} ($4f^0$) to Ce^{+3} ($4f^1$) implies the entry of an extra electron into *4f* orbitals [16]. This kind of orbital filling may reduces the intensity of peak *P* in the Ce M_5-edge and increase the $Ce^{+3}/(Ce^{+3}+Ce^{+4})$ ratio in the doped CeO_2 NPs. Hence, the changes in the $4f^0$ intensity (peak *P*) are consistent with the Ce^{+3} proportions that were estimated from the Ce M_5-edge (see Fig. 8 (a & b)).

To further understand the effect of doping on the local atomic structure of the as-synthesized NPs, systematic Ce K-edge EXAFS spectra were collected from the samples. The raw data were calibrated with the energy of Ce K-edge by using the Ce-foil. Background noise correction and normalization of the raw data were done by using Athena D-meter program package [27]. To investigate the atomic structure and relative bond length with respective to the absorbing atoms, the EXAFS data was Fourier transformed (FT) to *r*-space. To further simulate the FT data (in *r*-space) systematic theoretical structure of CeO_2 was generated by using the ATOM and FEFF codes [28]. The data range taken for the transformation is from 2.4 to 10.5 $Å^{-1}$ in *k*-space. Structural parameters were obtained from fitting in r-space, within the interval of 1.2-6 Å. The FT of k^3-weighted $\chi(k)$ for Ce K-edge EXAFS of as-synthesized samples are shown in Fig. 9. The weighted EXAFS data were transformed in to r-space and resultant back-transformed data along with the fit are shown in the Fig. 9. The shell parameters (coordination number (CN), bond-distance (R) and Debye-Waller factor (σ^2)) are presented in the Table 1. The first and second shells in the FTs are from the single scattering paths, Ce-O and Ce-cations (cations = Ce, Hf, Zr), respectively [21]. The third FT peak contains single and multiple scattering contributions from a variety of paths such as Ce-O, Ce-cation, Ce-cations-O, etc. Therefore, larger uncertainties in the third shell fitted parameters have been observed [21, 29] and thus the third shell (Ce-O) parameters may not useful in the present study too. Here, we first focus on the cation-cation network from the FT analysis of Ce K-edge EXAFS spectra and Table 1. The Ce-cation shell of the CeO_2 NPs was fitted with a single Ce-Ce bond. The structure parameters (CN = 11.85 and R = 3.846) are consistent with the value for the typical CeO_2 powders [29].

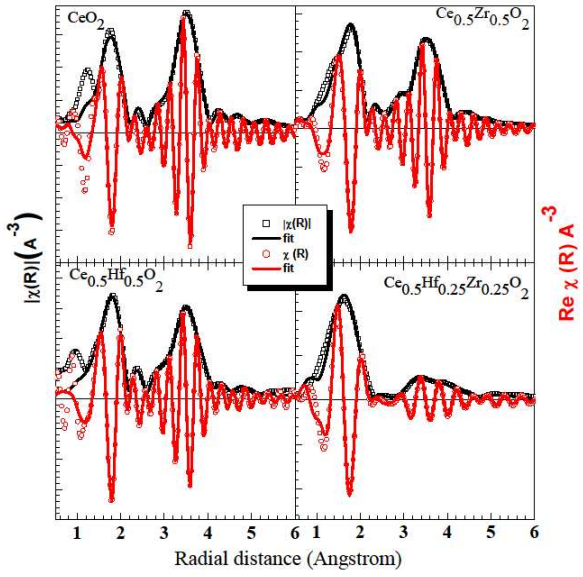

Fig. 9. (colour online) Radial distribution functions, obtained from Ce K-edge EXAFS data, of the CeO_2, $Ce_{0.5}Zr_{0.5}O_2$, $Ce_{0.5}Hf_{0.5}O_2$ and $Ce_{0.5}Hf_{0.25}Zr_{0.25}O_2$ NPs. (All of the Fourier transform curves are presented without phase correlation).

Table 1. Structural parameters (obtained from the Ce K-edge EXAFS data analysis) of first two coordination shells around Ce in CeO_2, $Ce_{0.5}Zr_{0.5}O_2$, $Ce_{0.5}Hf_{0.5}O_2$ and $Ce_{0.5}Hf_{0.25}Zr_{0.25}O_2$ NPs.

Sample	$Bond_{(shell)}$	CN	R(Å)	σ^2(Å^2)
CeO_2	$Ce-O_{(I)}$	8.043	2.3380	0.0086
	$Ce-Ce_{(II)}$	11.850	3.8460	0.0073
$Ce_{0.5}Zr_{0.5}O_2$	$Ce-O_{(I)}$	8.112	2.3291	0.0011
	$Ce-Zr_{(II)}$	6.281	3.8762	0.0105
	$Ce-Ce_{(II)}$	6.132	3.8425	0.0091
$Ce_{0.5}Hf_{0.5}O_2$	$Ce-O_{(I)}$	8.121	2.3255	0.0102
	$Ce-Hf_{(II)}$	6.261	3.8849	0.0324
	$Ce-Ce_{(II)}$	6.313	3.8412	0.0047
$Ce_{0.5}Hf_{0.25}Zr_{0.25}O_2$	$Ce-O_{(I)}$	8.124	2.3225	0.0087
	$Ce-Hf_{(II)}$	4.161	3.6972	0.0111
	$Ce-Zr_{(II)}$	3.869	3.6064	0.0116
	$Ce-Ce_{(II)}$	4.086	3.8322	0.0023
CeO_2 [Ref. 29]	$Ce-O_{(I)}$	8	2.344	0.0069
	$Ce-Ce_{(II)}$	12	3.827	0.0498

For the $Ce_{0.5}Hf_{0.5}O_2$ NPs, the Ce-cation shell was fitted with Ce-Ce (CN = 6.313, R = 3.841) and Ce-Hf (CN = 6.261, R = 3.884). Similarly, the Ce-cation shell of $Ce_{0.5}Zr_{0.5}O_2$ sample was fitted with Ce-Ce (CN = 6.132, R = 3.842) and Ce-Zr (CN = 6.281, R = 3.876). The CN ratio of Ce-Ce/Ce-Hf bonds and Ce-Ce/Ce-Zr bonds is close to *1* which is equal to Ce/Hf and Ce/Zr composition ratio in their respective samples (i.e., Hf in $Ce_{0.5}Hf_{0.5}O_2$ NPs and Zr in $Ce_{0.5}Zr_{0.5}O_2$ NPs). These results tally with the EDS data and strengthened the formation of good quality solid-solution samples of CeO_2 with Hf and Zr doping. Finally, the Ce-cation shell of $Ce_{0.5}Hf_{0.25}Zr_{0.25}O_2$ sample was fitted with Ce-Ce (CN = 4.086, R = 3.832), Ce-Hf (CN = 4.161, R = 3.697) and Ce-Zr (CN = 3.869, R = 3.606) bonds. In this case the CN ratio of the bonds is not consistent with the composition ratio of the elements in the sample. This indicates that, although Hf and Zr takes cations sites in the CeO_2 lattice, there remain Ce, Hf and Zr rich domains in the sample. Such structural perturbations lead to degradation of crystalline quality of the sample and are evidenced by the XRD measurements. Now we consider on the environment of O around the Ce in all the as-synthesized NPs. The CN and R of Ce-O bonds for pure CeO_2 NPs are very close to the respective values those for the typical CeO_2 powders [21, 29]. However, the Ce-O bond distance is found to be less and the CN is little higher in the case of Hf and Zr doped NPs. The ionic radius of Hf^{+4} and Zr^{+4}, for an 8-fold coordination, are smaller than that of Ce^{+4}. Therefore, shorter Ce-O bond length has been observed in the doped samples.

To further probe the local structure around the Zr and Hf atoms, systematic, EXAFS spectra were also collected at the Zr K-edge and Hf L_3-edge. Since, in the CeO_2 lattice, each Ce atom is situated amidst of eight O atoms and form MO_8 (M is metal atom) type polyhedra. Therefore, any substitution of Ce by Hf or Zr will also provide the same MO_8 type environment for Hf and Zr. Therefore, theoretical cubic ZrO_2 and HfO_2 structure were generated by using the ATOM and FEFF codes [28]. In such calculations, all the fitting parameters were kept similar to that of used in the Ce K-edge EXAFS data fittings. Fig. 10 shows the FT of the k^3-weighted $\chi(k)$ (uncorrected for phase shift), along with the theoretical fitted curves of (a) $Ce_{0.5}Zr_{0.5}O_2$, (b) $Ce_{0.5}Hf_{0.25}Zr_{0.25}O_2$ ((a) and (b) were obtained from the Zr K-edge EXAFS), (c) $Ce_{0.5}Hf_{0.5}O_2$ and (d) $Ce_{0.5}Hf_{0.25}Zr_{0.25}O_2$ ((c) and (d) were obtained from the Hf L_3-edge EXAFS). The noticeable change in the Fig. 10 is the reduction in the amplitude of FT intensity in the binary doped samples. This reduction in the

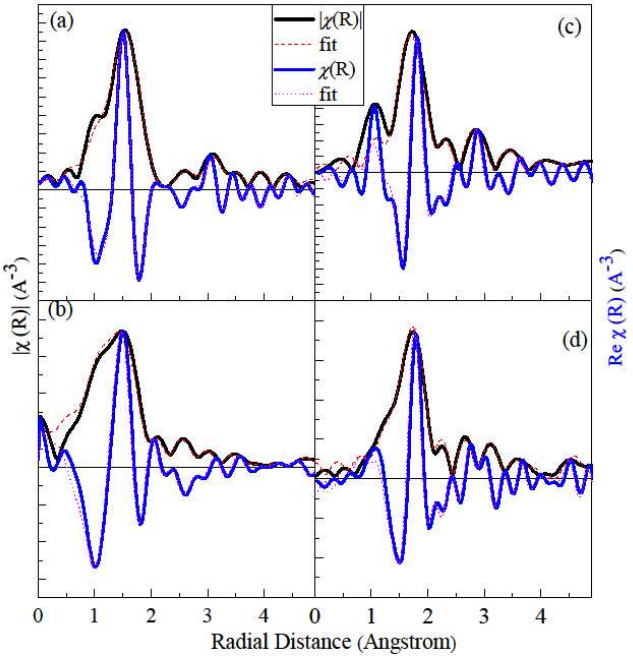

Fig. 10. (colour online) Radial distribution functions; (a) $Ce_{0.5}Zr_{0.5}O_2$ and (b) $Ce_{0.5}Hf_{0.25}Zr_{0.25}O_2$ NPs, (c) $Ce_{0.5}Hf_{0.5}O_2$ and (d) $Ce_{0.5}Hf_{0.25}Zr_{0.25}O_2$ NPs. ((a)-(b) are obtained from the Zr K-edge EXAFS data analysis and the (c)-(d) are obtained from the Hf L_3-edge EXAFS analysis).

amplitude of FT intensity could be ascribed to the defective crystalline lattice in the doped samples [30-31]. CN, R, and σ^2 were obtained from the EXAFS analysis of Zr K and Hf L_3-edges and tabulated in the Table 2. It is clear from the table 2 that the Zr-Ce, and Hf-Ce bond distances, obtained from the Zr K-edge and Hf-L_3-edge EXAFS fitted data, are close to that of estimated from the Ce K-edge EXAFS data fittings. However, the Zr-O and Hf-O distances were found to little higher in the doped samples. In the previous reports, larger Zr-O and Hf-O bond distances have been reported in the tetragonal/cubic ZrO_2 and HfO_2, compared with the monoclinic structure [31-33]. In the present case the Zr and Hf atoms are supposed to occupy the cubic environment of CeO_2 lattice and form MO_8 type pylyhedra. This may result in larger Zr-O and Hf-O distances, observed in the present case. For all the EXAFS data fittings, the value of the σ^2 is better than the reported values [29-33] and thus signifies the best fittings of the present data. In the present case, we believe that the unlike formation of secondary phases and substitutional doping of Hf and Zr in the CeO_2 lattice (as convinced by XRD, NEXAFS and EXAFS data) lead to variation in the CN and R of CeO_2 NPs, and thus modify the electronic structure (i.e., 4*f* occupancy and $Ce^{+3}/(Ce^{+3}+Ce^{+4})$ ratio*)* of the compounds.

Conclusions

Pure, Zr, Hf and Hf+Zr doped CeO_2 NPs were synthesized using the co-precipitation method. Significant peak broadening and decrease in the average grain size was observed in the XRD analysis but the TEM images depict the formation of spherical shaped NPs of ~ 5 nm in diameter. The elemental concentration in the samples, determined by the EDS data, was nearly the same as used during the synthesis procedure. The energy separation between the t_{2g} and e_g peaks in the O K-edge NEXAFS spectra of the Zr and Hf doped NPs did not changed according to the grain size variation and thus nullifies the grain size effects in electronic structure properties of the as-synthesized samples. Detailed analysis on the pre-edge peak in the O K-edge spectra and post-

Table 2. Structural parameters (obtained from the Zr K-edge and Hf L_3-edge EXAFS data analysis) of first two coordination shells around Zr and Hf atoms in $Ce_{0.5}Zr_{0.5}O_2$, $Ce_{0.5}Hf_{0.5}O_2$ and $Ce_{0.5}Hf_{0.25}Zr_{0.25}O_2$ NPs.

Sample (EXAFS edge)	Bond$_{(shell)}$	CN	R(Å)	σ^2(Å^2)
$Ce_{0.5}Zr_{0.5}O_2$ (Zr K-edge)	Zr-$O_{(I)}$	8.107	2.283	0.0065
	Zr-$Zr_{(II)}$	6.312	3.617	0.0121
	Zr-$Ce_{(II)}$	6.021	3.791	0.0074
$Ce_{0.5}Hf_{0.5}O_2$ (Hf L3-edge)	Hf-$O_{(I)}$	7.936	2.279	0.0031
	Hf-$Hf_{(II)}$	5.937	3.783	0.0152
	Hf-$Ce_{(II)}$	6.211	3.815	0.0078
$Ce_{0.5}Hf_{0.25}Zr_{0.25}O_2$ (Zr K-edge and Hf L3-edge)	Zr –$O_{(I)}$	8.032	2.219	0.0031
	Hf-$O_{(I)}$	8.104	2.208	0.0059
	Hf –$Ce_{(II)}$	4.231	3.824	0.0084
	Zr-$Ce_{(II)}$	4.021	3.804	0.0068
m-HfO_2 [Ref. 32]	Hf-$O_{(I)}$	7	2.144	0.0151
	Hf-$Hf_{(II)}$	12	3.435	0.0227
c-ZrO_2 [Ref. 31]	Zr-$O_{(I)}$	8	2.222	-0.0081
	Zr-$Zr_{(II)}$	12	3.628	0.0061

edge peak in Ce $M_{5,4}$-edge spectra have shown higher $Ce^{+3}/Ce^{+3}+Ce^{+4}$ ratio in the Hf and Zr doped CeO_2 NPs. The local atomic structure around the Ce, Zr and Hf atoms was investigated by EXAFS spectroscopy at Ce K-edge, Zr K-edge and Hf L_3-edge, respectively. The CN ratios of second shell Ce-Ce/Ce-Hf and Ce-Ce/Ce-Zr bonds were approximately 1 which is equal to the Ce/Hf and Ce/Zr compositional ratio in their respective samples. The first shell Ce-O distance was found to be slightly shorter for all the doped NPs, indicating contraction of the lattice with Hf and Zr doping. The Ce-Ce, Ce-Zr and Ce-Hf bond distanced measured by the Ce K-edge EXAFS fittings tally with the Zr K-edge and Hf L_3-edge EXAFS analysis and strengthened the view of the formation of Zr and Hf substituted CeO_2 NPs.

Acknowledgement

Aditya Sharma and H. J. Shin would like to acknowledge the financial support by the Basic Science Research Program (No. 2008-0062606, CELA-NCRC) through the National Research Foundation of Korea (NRF) and by the Converging Research Center Program (2013K000306), funded by the Korea government Ministry of Science, ICT and Future Planning (MSIP).

Notes and references

[a] *Pohang Accelerator Laboratory, POSTECH, Pohang – 790-784, South Korea. Fax: +82-54279-1599; Tel: +82-54279-1767; E-mail: adityaiuac@gmail.com, shj01@postech.ac.kr*

[b] *Advanced Analysis centre, Korea Institute of Science and technology, Seoul -136-791, South Korea.*

[ψ] *Presently at: SSB UICET, Panjab University Chandigarh 160-014, India; E-mail: sgautam@pu.ac.in*

1. G. Kalkowski, C. Laubschat, W. D. Brewer, E.V. Sampathkumaran, M. Domke and G. Kaindl, Phys. Rev. B, 1985, **32**, 2717-2720.
2. T. Ghoshal, P. G. Fleming, J. D. Holmes and M. A. Morris, J. Mater. Chem., 2012, **22**, 22949-22957.
3. V. Stetsovych, F. Pagliuca, F. Dvorak, T.Duchon, M. Vorokhta, M. Aulicka, J. Lachnitt, S. Schernich, I. Matolinova, K. Veltruska, T.Skala, D. Mazur, J. Myslivecek, J. Libuda, and V. Matolin, J. Phys. Chem. Lett. 2013, **4**, 866−871.
4. C.T. Campbell and C. H.F. Peden, Science, 2005, **309**, 713-714.
5. Q.Fu, H. Saltsburg, M. F. Stephanopoulos, Science, 2003, **301**, 935-938.
6. Z. Zhan and S. A. Barnett, Science, 2005, **308**, 844-847.
7. A. Sundaresan, and C.N.R. Rao, Nano Today, 2009, **4**, 96-106.
8. M. Y. Ge, H. Wang, E. Z. Liu, J. F. Liu, J. Z. Jiang, Y. K. Li, Z. A. Xu, and H. Y. Li, Appl. Phys. Lett., 2008, **93**, 062505-062507.
9. T. Baidya, A. Gupta, P. A. Despandey, G. Madras and M. S. Hegde, J. Phys. Chem. C, 2009, **113**, 4059-4068.
10. M. Shen, J. Wang, J. Shang, Y. An, J. Wang and W. Wang, J. Phys. Chem. C, 2009, **113**, 1543-1551.
11. B.M. Reddy, L. Katta and G. Thrimurthulu, Chem. Mater., 2010, **22**, 467-475.
12. Q. Dong, S. Yin, C. Guo and T. Sato, Nano. Res. Lett. 2012, **7**, 542-546.
13. G.L. Jose, A. Rodriguez, Z. Chang and J. Hrbek, J. Phys. Chem. B, 2004, **108**, 2931-2938.
14. T. Baidya, M. S. Hegde and J. Gopalakrishnan, J. Phys. Chem. B, 2007, **111**, 5149-5154.
15. A. Gupta, M.S. Hegde, K.R. Priolkar, U.V. Waghmare, P.R. Sarode, and S. Emura, Chem. Mater, 2009, **21**, 5836.
16. W. C. Wang, S. Y. Chen, P. A. Glans, J. Guo, R. Chen, K. W. Fong, C. L. Chen, A.Gloter, C. Lin Chang, T.S. Chan, J. M. Chen, J. F. Leed and C. L. Dong, Phys. Chem. Chem. Phys., 2013, **15**, 14701-14707.
17. A. B. Kehoe, D. O. Scanlon and G. W. Watson, Chem. Mater. 2011, **23**, 4464-4468.
18. M. Pal, U. Pal, J. M. Gracia, Y. Jimenez and Felipe Perez-Rodrrguez, Nano. Res. Lett., 2012, **7**, 1-12.
19. F. Zhang, P. Wang, J. Koberstein, S. Khalid, S.W. Chan, Surf. Sci. 2004, **563**, 74-82.
20. X. Wang, J.C. Hanson, and J. A. Rodriguez, J. Chem. Phys. 2005, 1**22**, 154711-154721.
21. J. F. Lee, M.T. Tang, W. C. Shin and R. S. Liu, Mat. Res. Bul., 2002, **37**, 555-562.
22. A. Sharma, A. P. Singh, P. Thakur, N. B. Brookes, S. Kumar, C. G. Lee, R. J. Choudhary, K. D. Verma, and R. Kumar, J. Appl. Phys., 2010, **107**, 093918-093925.
23. M. Varshney, A. Sharma, K. D. Verma and R. Kumar, Phys. Scr., 2012 **86,** 015605-015612.
24. J. G. Chen, Surf. Sci. Reports. 1997, **30**, 1-152.
25. J. A. Rodriguez, J. C. Hanson, J.Y. Kim, G. Liu, A.I. Jues, and M.F. Garcia, J. Phys. Chem. B, 2003, **107**, 3535-3543.
26. S. O. Kucheyev, B.J. Clapsaddle, Y. M. Wang, T.V. Buuren and A.V. Hamza, Phys. Rev. B, 2007, **76**, 235420-235425.
27. B. Ravel, M. Newville, J. Synch. Rad. 2005, **12**, 537–541.
28. A. L. Ankudinov, and J. J. Rehr, Phys. Rev. B, 1997, **56**, R1712-R1715.
29. P. Nachimuthu, W.C. Shin, R.S. Liu, L.Y. Jang and J. M. Chen, J. Solid State Chem. 2000, **149**, 408-413.
30. S. Kumar, S. Gautam, T. K. Song, K. H. Chae, K. W. Jang and S. S. Kim, J. Alloy, Compound. 2014, **611**, 329-334.
31. Y. Nagai, T. Nonaka, A. Suda, M. Sugiura, R&D Rev. Toyota 2002, **37**, 20-27.
32. N.D. Afify, G. Dalba, U. M. K. Koppolu, C. Armellini, Y. Jestin and F. Rocca, Mat. Sci. Semicond. Proc. 2006, **9**, 1043-1048.
33. P. S. Lysaght, J. C. Woicik, M. A. Sahiner, B. H. Lee, R. Jammy, Appl. Phys. Lett. 2007, **91**, 122910.